Fermi arcs for generic nodal points hosting monopoles or dipoles

Ipsita Mandal*
Department of Physics, Shiv Nadar Institution of Eminence (SNIoE), Gautam Buddha Nagar, Uttar Pradesh 201314, India

Fermi arcs represent the surface states at the boundary of a three-dimensional topological semimetal with the vacuum, illustrating the notion of bulk-boundary correspondence playing out in real materials. Their special character is tied up with the topological charges carried by the nodes of the semimetal in the momentum space, where two or more bands cross. In fact, they are constrained to begin and end on the perimeters of the projections of the Fermi surfaces of the bands tangentially, signalling their mixing with the bulk states. The number of Fermi arcs grazing onto the tangents of the outermost projection about a given node also reflects the magnitude of the charge at the node (equalling the Berry-curvature monopole), revealing the intrinsic topology of the underlying bandstructure, which can be visualised in experiments like ARPES. Here we take upon the task of unambiguously characterising the analytical structure of these states for generic nodal points, (1) whose degeneracy might be twofold or multifold; and (2) the associated bands might exhibit isotropic or anisotropic, linear- or nonlinear-in-momentum dispersion. Moreover, we also address the question of whether we should get any Fermi arcs at all for topological nodes carrying zero values of monopoles, but representing ideal dipoles.

CONTENTS

I. INTRODUCTION

Three-dimensional (3d) semimetals harbouring defective points in the Brillouin zone (BZ), where $(2\varsigma + 1)$ cross at a nodal-point degeneracy [see Fig. 1(a)], provide an intriguing crucible to observe mathematical notions of topology playing out in real-life systems [1–6]. In the vicinity of a nodal point, the bands form a spin-ς representation of the SU(2) group, being represented as the effective Hamiltonian, $\boldsymbol{d}(\boldsymbol{k}) \cdot \boldsymbol{S}$, with $\boldsymbol{d}(\boldsymbol{k}) = \{d_x(\boldsymbol{k}), d_y(\boldsymbol{k}), d_z(\boldsymbol{k})\}$. Here, $\mathbf{k} = \{k_x,\, k_y,\, k_z\}$ labels the 3d BZ and $\boldsymbol{S}$ indicates the vector operator comprising the components $\{S_x,\, S_y,\, S_z\}$. Thus, $\boldsymbol{S}$ acts as the well-known angular-momentum operators. The bands are labelled with the eigenvalues of S_z, spanning from $-\varsigma$ to ς, which are conventionally referred to as the pseudospin quantum numbers (distinct form the actual spin quantum numbers of the electrons). The simplest representative system is an isotropic Weyl node, appearing in semimetals (WSMs) [1, 2], carrying $\varsigma = 1/2$ via its two bands. Needless to say, we have now its multifold cousins like the triple-point semimetals (with $\varsigma = 1$) and Rarita-Schwinger-Weyl (RSW) nodes (with $\varsigma = 3/2$) [4, 5, 7–12]. The connection with topology is encoded in

* ipsita.mandal@snu.edu.in

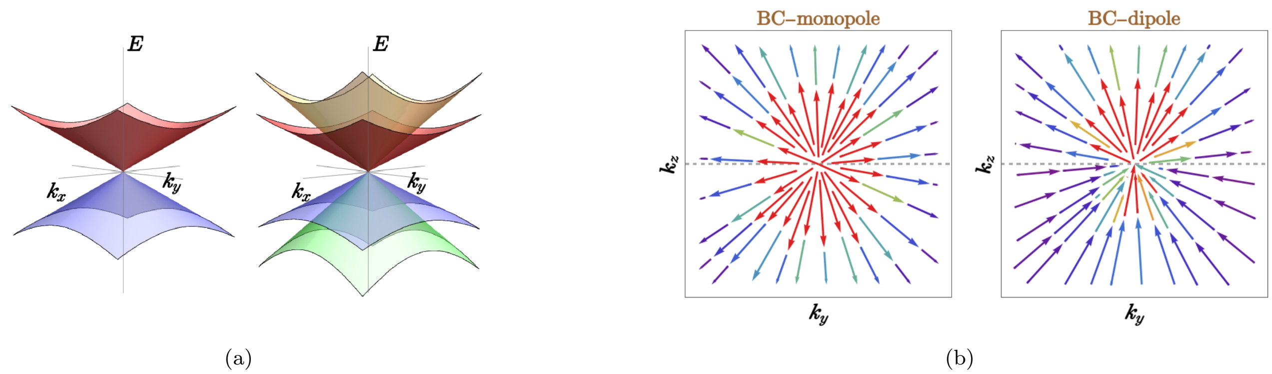

FIG. 1. (a) Dispersion (E) in isotropic twofold (viz. Weyl node) and fourfold (viz. Rarita-Schwinger-Weyl node) band-crossings against the $k_x k_y$-plane. (b) Schematics of BC-flux lines in the $k_x = 0$ planes for a monopole and an ideal dipole. Here, the dipole-axis is orientied along the k_z-axis and, hence, the BC goes to zero on the $k_z = 0$ plane in the 3d BZ.

the quantum-mechanical phase embodied by the Berry phase, which gives rise to topological vector fields like the Berry curvature (BC) and the intrinsic orbital magnetic moment (OMM) in the momentum space [13]. In fact, the nodes act as sources/sinks of the flux of the BC-vector field [cf. Fig. 1(b)], which explains their singular nature. The magnitude of the BC-monopole carried by a nodal point is synonymous with the Chern number of any closed 2d surface (in momentum space) containing the node inside, giving us the associated topological invariant in terms of the BC-monopole charge. Beyond this simple picture, we are also now aware of more possibilities of the behaviour of the BC where the nodes act as source of higher-order poles [14–16] (for instance, ideal dipoles, quadrupoles, and so on), thus mimicking our well-known concepts (arising from multipole expansions) of electromagnetism.

Saliently, the existence of the intrinsic topology in the 3d BZ, when treated as a 3d manifold, is reflected in various physical quantities, which can be detected via contemporary experimental techniques. One example is the various types of response that can be detected in transport-measurements, which have been theoretically understood and realised experimentally [3, 6, 12, 17, 18]. The list comprises diverse effects such as intrinsic anomalous-Hall effects [19–21], planar-Hall and Hall coefficients [6, 12, 17, 18, 22–31], Magnus-Hall effects [32], circular dichroism [33], and circular photogalvanic effect [34–36]. However, we must emphasise that perhaps the most unambigous signature comprises the Fermi arcs [37–44], which can be cleanly visualised in experiments like angle-resolved photoemission spectroscopy (ARPES). They represent the surface states in a two-dimensional (2d) surface Brillouin zone (SBZ), always ending tangentially on the boundaries of the projections of the Fermi-surfaces (FSs) of the various bands, where they merge and disappear into the bulk states.

The Fermi arcs are interpreted as the locii of the surface states when we take a surface (say, whose outward normal is along the normal is along the unit vector, $\hat{\boldsymbol{n}}$) of a slab consisting of the semimetallic material. In fact, these surface states arise due to the presence of chiral edge modes in 2d slices of the 3D BZ, after we impose open boundary conditions on those slices [1, 2]. Although we can no longer describe the system in the momentum space for the direction along $\hat{\boldsymbol{n}}$, the momentum-components perpendicular-to-$\hat{\boldsymbol{n}}$ (say, $\mathbf{k}_{\parallel}$), i.e., parallel to the surface itself, remain good quantum numbers (as long as we consider very large spatial dimensions along those directions). Thus, a single (boundary) surface in real space gives us an SBZ, spanned by the components of $\mathbf{k}_{\parallel}$, and hosting the Fermi arcs. Although the analytical derivation of surface states, which take the form of Fermi arcs in nodal-point semimetals, is well-understood for the case of Weyl semimetals [45–48], for most other cases, the derivations are system-specific and not generic-enough [45, 49–53] to be applicable for arbitrary cases of dispersion (for example, anisotropic and/or nonlinear-in-momentum behaviour) and band-crossings. In this paper, our aim is to outline a generic procedure to obtain the analytical forms of the Fermi arcs, which also reflect the Chern numbers of the corresponding 2d slices whose edge states they represent when bulk-boundary correspondence is invoked [1, 2].

The paper is organised as follows: In Sec. II, we lay out our formulation of the boundary conditions, which leads to the solution for the surface states for a generic nodal-point semimetal. Sec. III is devoted to the application of our method to diverse systems, spanning twofold to multifold ones, linear-in-momentum to quadratic- and cubic-in-momentum ones, and isotropic to anisotropic ones. Furthermore, we also consider two cases where the nodal points represent ideal BC-dipoles rather than monopoles. Finally, we end with a summary and outlook in Sec. IV.

II. FORMULATION OF BOUNDARY CONDITIONS

Let us take a single surface at $x = 0$ such that the $x < 0$ region represent a semi-infinite semimetal, with the bulk Hamiltonian $H(\mathbf{k})$, where $\mathbf{k} \equiv \{k_x, k_y, k_z\}$ and $k = \sqrt{k_x^2 + k_y^2 + k_z^2}$. The translation symmetry is broken along the x-axis, and we use the Hamiltonian,

$$H_x = H(k_x \to -i\,\partial_x, k_y, k_z)\,. \tag{1}$$

Demanding that H_x be Hermitian in the region $x \in [0,\infty)$, we have the physical condition that

$$\int_0^\infty dx\,\psi^\dagger(x)\,H_x\,\phi(x) = \int_0^\infty dx\,[H_x\,\psi(x)]^\dagger\,\phi(x)\,, \tag{2}$$

while considering two bonafide boundary-states, ψ and ϕ. The current-density operator is defined as

$$j_x \equiv \partial_{k_x} H(\mathbf{k})|_{k_x\to -i\,\partial_x}\,. \tag{3}$$

Consequently, Eq. (2) also translates into a physically-sensible boundary condition (bc) which prohibits the current transmission through the boundary via $(\psi^\dagger\, j_x\,\psi)|_{x=0} = 0$, alternatively known as the hard-wall bc. The boundary modes must behave as decaying wavefunctions of the form of

$$\psi(x) = \psi_0\, e^{-\kappa\, x} \text{ with } \mathrm{Re}(\kappa) > 0\,, \tag{4}$$

so that the surface states are bound to the boundary at $x = 0$. Here, ψ_0 is independent of x and any x-dependence of $\psi(x)$ is assumed to be contained in the $e^{-\kappa\,x}$ factor.

A. Witten's formulation for an untilted Weyl node

The effective Hamiltonian in the vicinity of a single Weyl node [cf. Fig. 1(a)] is captured by

$$H_W(\mathbf{k}) = \boldsymbol{\sigma}\cdot\mathbf{k}\,. \tag{5}$$

Eq. (2) translates into

$$\psi^\dagger(x)\,\sigma_x\,\phi(x)|_{x=0} = 0 \Rightarrow j_x|_{x=0} \equiv \psi_0^\dagger\,\sigma_x\,\phi_0 = 0\,. \tag{6}$$

An energy-independent boundary condition can be formulated as a local linear restriction on the components of the spinor wave function at the boundary, captured by [45]

$$\Psi_0 = M\,\Psi_0\,,\ \text{where } M = \cos\alpha\,\sigma_y + \sin\alpha\,\sigma_z\,. \tag{7}$$

This is a good boundary condition because σ_x anticommutes with M, leading to

$$\psi_0^\dagger\,\sigma_x\,\phi_0 = \frac{1}{2}\left[\psi_0^\dagger\,\sigma_x\,M\,\phi_0 + (M\,\psi_0)^\dagger\,\sigma_x\,\phi_0\right] = 0\,. \tag{8}$$

The variable α acts as a parameter and, by changing α, we get Fermi arcs of various shapes and orientations with the restriction that they originate tangentially from the boundary of the projection of the FS on the $k_y k_z$-plane.

B. Generic formulation applicable for any kind of nodes

For generic nodes with multifold nodes and/or nonlinear powers of the components of $\mathbf{k}$, Witten's trick will not work, which we will explicitly see why considering some specific examples. Hence, we need an unambigous generic method applicable to derive the equations describing the curves representing the relevant Fermi arcs, which we describe here. Suppose we have an N-fold degeneracy at a node, described by the $N\times N$ Hamiltonian, $H_N(\mathbf{k})$ in the bulk BZ. Let us look for surface states where the surface-normal is along the direction denoted by the unit vector, $\hat{\boldsymbol{n}}$, and located at $r_\perp = 0$, where $r_\perp \equiv \mathbf{r}\cdot\hat{\boldsymbol{n}}$. We set our convention that the region $r_\perp < 0$ represents the region occupied by the semimetallic material, while $r_\perp > 0$ represents the adjoining non-topological region (e.g., vacuum). Dividing up the momentum components along and perpendicular to $\hat{\boldsymbol{n}}$ as $k_\perp$ and $\mathbf{k}_\parallel$, the boundary Hamiltonian is obtained as

$$H_{r_\perp} = H_N(k_\perp \to -i\,\partial_{r_\perp}, \mathbf{k}_\parallel)\,. \tag{9}$$

The imposition of the Hermiticity condition on $H_{r_\perp}$ leads to

$$\int_0^\infty dr_\perp\,\psi^\dagger(r_\perp)\,H_{r_\perp}\,\phi(r_\perp) = \int_0^\infty dr_\perp\,[H_{r_\perp}\,\psi(r_\perp)]^\dagger\,\phi(r_\perp)\,, \tag{10}$$

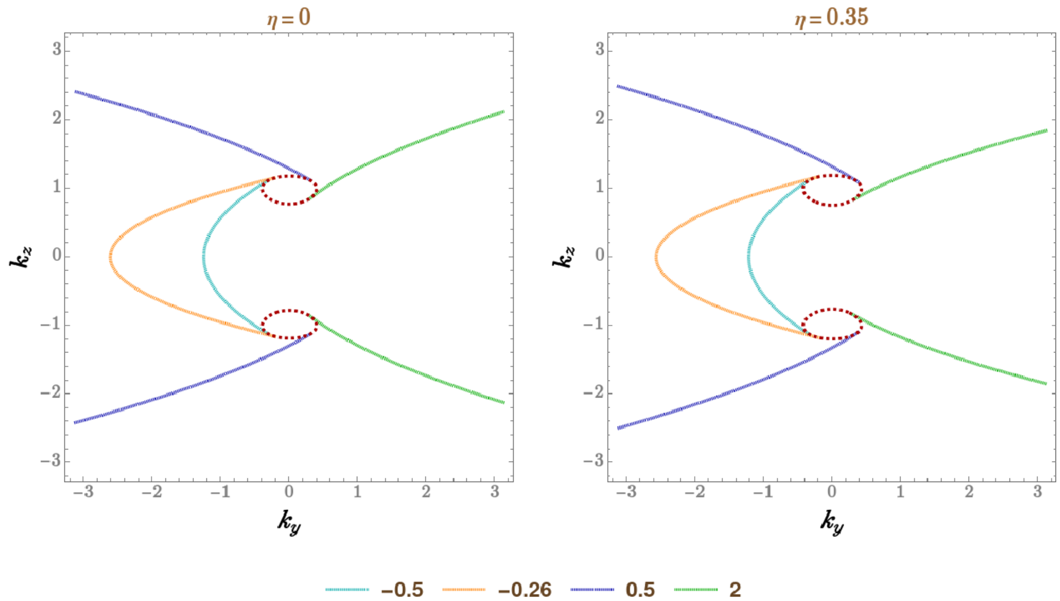

FIG. 2. A pair of conjugate Weyl nodes: The Fermi arcs represent modes with $E = \mu$, where $\mu = 0.5$ and $k_w = 1$. Each arc corresponds to a distinct value of b_1, colour-coded as shown in the plot-legends. The dashed red curves represent the projections of the bulk FSs on the $k_y k_z$-plane.

analogous to Eq. (2). Let us parametrise a solution as

$$\psi(r_\perp) = \psi_0 \, e^{-\kappa \, r_\perp} \text{ with } \mathrm{Re}(\kappa) > 0 \text{ and } \psi_0^T = \begin{bmatrix} 1 & a_1 + i\, b_1 & a_2 + i\, b_2 & \cdots & a_{N-1} + i\, b_{N-1} \end{bmatrix} . \tag{11}$$

As argued earlier, (after some manipulations involving integration by parts to convert the integrands into total derivatives) Eq. (10) will turn out to be equivalent to the condition of

$$\psi^\dagger(r_\perp)\, j_{r_\perp} \psi(r_\perp)\big|_{r_\perp = 0} = 0 \,, \text{ where } j_{r_\perp} \equiv \partial_{k_\perp} H_N(k_\perp, \mathbf{k}_\parallel)\big|_{k_\perp \to -i\,\partial_{r_\perp}} \tag{12}$$

represents the current-density operator perpendicular to the surface. Next, we need to solve for the eigenvalue equation,

$$H_{r_\perp} \psi(r_\perp) = E\, \psi(r_\perp) \,, \tag{13}$$

which leads to N complex-valued equations involving the $(2N+1)$ unknown variables E, $\kappa_r \equiv \mathrm{Re}(\kappa)$, $\kappa_i \equiv \mathrm{Im}(\kappa)$, a_1, b_1, a_2, b_2, $\cdots$, a_{N-1}, and b_{N-1}. This implies that we have $(2N+1)$ real equations [on including the real equation coming from Eq. (12)] at our disposal, which we can use to solve for the same number of unknown variables. In the next section, we will study a variety of systems to see that the above procedure works generically.

III. SPECIFIC EXAMPLES

In this section, we will take some specific systems spanning generic features like nonlinear dispersion and multifold band-crossings. In the process, we will also observe how the emergent Fermi arcs reflect the underlying Chern numbers (or, equivalently, monopole charges) of the associated nodes. Additionally, we resolve the issue whether Fermi arcs can appear in nodes harbouring ideal BC-dipoles.

A. Untilted nodes of a Weyl semimetal

Let us consider the one-node model given by Eq. (5), where we want to consider a boundary at $x = 0$, indicating $\hat{\boldsymbol{n}} = \hat{\boldsymbol{x}}$. Using $\psi_0^T = \begin{bmatrix} 1 & a_1 + i\, b_1 \end{bmatrix}$, Eq. (6) yields $a_1 = 0$. Next, the two components of the matrix equation in Eq. (13) take the forms of

$$b_1 \left(-i\, \kappa_i + k_y - \kappa_r\right) - E + k_z = 0 \text{ and } -b_1 \left(E + k_z\right) + i\, \kappa_i + k_y + \kappa_r = 0$$
$$\Rightarrow b_1 \left(k_y - \kappa_r\right) - E + k_z = 0 \,, \quad b_1\, \kappa_i = 0 \,, \quad \kappa_i = 0 \,, \text{ and } -b_1 \left(E + k_z\right) + k_y + \kappa_r = 0 \,, \tag{14}$$

after decomposing them into real and imaginary parts. We obtain the solutions as $E = \frac{2\,b_1\,k_y+(1-b_1^2)\,k_z}{1+b_1^2}$, $\kappa_r = \frac{(b_1^2-1)k_y+2\,b_1\,k_z}{1+b_1^2}$, and $\kappa_i = 0$. We find that b_1 plays the role of a parameter, just like α in Eq. (7). The range of the Fermi arc is determined by the region where $\kappa_r > 0$, i.e., $\left(b_1^2-1\right)k_y + 2\,b_1\,k_z > 0$. The arcs end tangentially on the projections of the bulk FSs, mixing with the bulk states, which is the point where k_y and k_z are as the solutions of the simultaneous equations, $E(k_y,k_z) = \mu$ and $\sqrt{k_y^2+k_z^2} = \mu$. One can check that at this point, $\{k_y,k_z\} = \frac{\mu}{1+b_1^2}\{2\,b_1,\,1-b_1^2\}$ $\Rightarrow \kappa_r = 0$. Therefore, the surface state ceases to exist at this point, merging with the bulk states.

For the case of two nodes, separated along the k_z-direction (for example) by an amount k_w, we can easily get the nature of the Fermi arcs by the replacement $k_z \to (k_z^2 - k_w^2)$. Fig. 2 illustrates the Fermi arcs for four distinct values of b_1, when the chemical potential μ cuts the bandstructure of the surface bands.

B. Tilted nodes of a Weyl semimetal

The bulk Hamiltonian in the vicinity of a node, tilted with respect to the k_x-axis, is captured by The effective Hamiltonian in the vicinity of a single Weyl node is captured by

$$H_W(\mathbf{k}) = \boldsymbol{\sigma}\cdot\mathbf{k} + \eta\,k_x\,\mathbb{I}_{2\times 2}\,. \tag{15}$$

For this case, on using $\psi_0^T = \begin{bmatrix}1 & a_1 + i\,b_1\end{bmatrix}$, Eq. (12) yields

$$\psi_0^\dagger\,\sigma_x\,\psi_0 + \eta\,\psi_0^\dagger\,\psi_0 = 0 \Rightarrow 2\,a_1 + \eta\left(1 + a_1^2 + b_1^2\right) = 0. \tag{16}$$

Next, the two components of the matrix equation shown in Eq. (13) take the forms of

$$\begin{aligned}
&i\,\kappa_r\,(a_1 + i\,b_1 + \eta) - a_1\kappa_i - i\,a_1\,k_y - i\,b_1\kappa_i + b_1\,k_y - E - \eta\,\kappa_i + k_z = 0\\
&\text{and } i\,(i\,\kappa_i + k_y + \kappa_r) - (a_1 + i\,b_1)\left[E + \eta\,(\kappa_i - i\,\kappa_r) + k_z\right] = 0\\
\Rightarrow &-(a_1+\eta)\,\kappa_i + b_1\,(k_y - \kappa_r) - E + k_z = 0\,, \quad -a_1\,k_y + (a_1+\eta)\,\kappa_r - b_1\,\kappa_i = 0\,,\\
&-a_1\,(E + \eta\,\kappa_i + k_z) - b_1\,\eta\,\kappa_r - \kappa_i = 0\,, \quad a_1\,\eta\,\kappa_r - b_1\,(E + \eta\,\kappa_i + k_z) + k_y + \kappa_r = 0\,.
\end{aligned} \tag{17}$$

We obtain the solutions as $E = \frac{b_1\left[\sqrt{1-\left(1+b_1^2\right)\eta^2}+1\right]k_y + \left[\sqrt{1-\left(1+b_1^2\right)\eta^2}-b_1^2\right]k_z}{1+b_1^2}$, $\kappa_r = \frac{\left(b_1^2-1\right)k_y+2\,b_1\,k_z}{1+b_1^2}$, $\kappa_i = 0$, and $a_1 = \frac{\sqrt{1-\left(1+b_1^2\right)\eta^2}-1}{\eta}$. While for the untilted case (i.e., $\eta = 0$), the projection is the locus of the curve $k = \mu$ at $k_x = 0$, for the tilted case (i.e., $\eta \neq 0$), it is the locus of the curve $k = \mu$ at $k_x = -\eta\sqrt{(k_y^2+k_z^2)/(1-\eta^2)}$ (or, equivalently, $k\sqrt{1-\eta^2} = \mu$ at $k_x = 0$). This is because, for $\mu \neq 0$, the anisotropic FS (having the shape like a spheroid elongated along the k_x-direction) has its largest radius of projection at a negative value of k_x. Consequently, the arcs end tangentially on the surface $\sqrt{(k_y^2+k_z^2)}\,\sqrt{1-\eta^2} = \mu$. Solving for k_y and k_z using $E(k_y,k_z) = \mu$ in conjunction, we obtain the coordinates of the Fermi-arc's ending as $\{k_y,k_z\} = \frac{\mu}{\left(1+b_1^2\right)(1-\eta^2)}\left\{b_1\left[1+\sqrt{1-(1+b_1^2)\,\eta^2}\right],\,\sqrt{1-(b_1^2+1)\,\eta^2}-b_1^2\right\}$, where of course κ_r goes to zero. Again, for the case of two nodes, separated along the k_z-direction (for example) by an amount k_w, we can easily get the nature of the Fermi arcs by the replacement $k_z \to (k_z^2 - k_w^2)$. Fig. 2 illustrates the Fermi arcs for the two-node case using four distinct values of b_1, with η set to 0.35.

C. Triple-point semimetal

Let us now consider bands carrying pseudospin-1 quantum numbers crossing at threefold-degenerate nodes [4, 5, 28, 29, 32, 54], representing the so-called triple-point semimetals (TSMs). These are three-band generalisations of the pseudospin-1/2 quasiparticles in Weyl semimetals, with the nodal points acting as Berry-curvature monopoles of magnitude 2. They can be realised in 3d tight-binding models for cold fermionic atoms in cubic optical lattices [55] and, via *ab initio* simulations, have been identified in materials like TaN, NbN, and WC-type ZrTe [54, 56–58]. The effective low-energy continuum Hamiltonian, in the vicinity of a threefold nodal point, is given by

$$\mathcal{H}_T(\mathbf{k}) = \mathbf{k}\cdot\boldsymbol{\mathcal{S}}\,. \tag{18}$$

Here, $\boldsymbol{\mathcal{S}}$ represents the vector spin-1 operator with three components,

$$\mathcal{S}_x = \frac{1}{\sqrt{2}}\begin{bmatrix}0 & 1 & 0\\ 1 & 0 & 1\\ 0 & 1 & 0\end{bmatrix}, \quad \mathcal{S}_y = \frac{1}{\sqrt{2}}\begin{bmatrix}0 & -i & 0\\ \mathrm{i} & 0 & -i\\ 0 & i & 0\end{bmatrix}, \quad \mathcal{S}_z = \begin{bmatrix}1 & 0 & 0\\ 0 & 0 & 0\\ 0 & 0 & -1\end{bmatrix}. \tag{19}$$

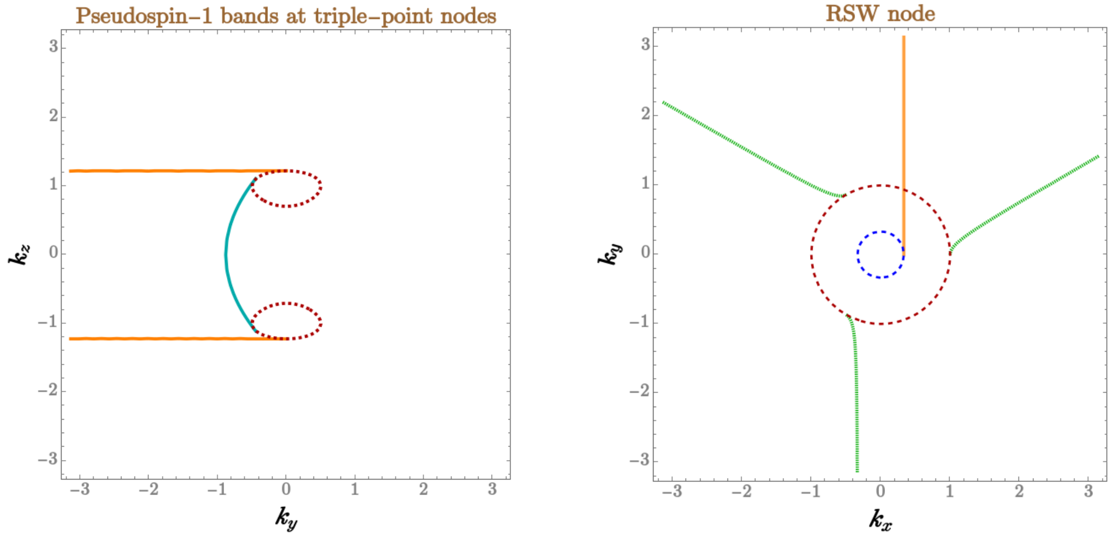

(a)

(b)

FIG. 3. (a) A pair of triple-point nodes: The Fermi arcs represent modes with $E = \mu$, where $\mu = 0.5$ and $k_w = 1$. The dashed red curves represent the projections of the bulk FSs (of the non-flat bands) on the $k_y k_z$-plane. The two Fermi arcs emanating tangentially from each FS-projection reflect the magnitude Chern number at each node equalling two. The cyan arc has been obtained by setting $b_1 = -1$. (b) Four Fermi arcs emerging from the FS-projects of the two conduction bands of an isotropic RSW node with $\mu = 0.5$ and $b_1 = 0$, indicating the Chern number to be four.

The Chern-number values of ± 2 indicate that we must have two distinct Fermi arcs associated with each node [40, 41].

Here we note that, although this is a straightforward generalisation of the isotropic Weyl node, we cannot apply Witten's method (outlined in Sec. II A) simply because of the fact that $\mathcal{S}_x$, $\mathcal{S}_y$, and $\mathcal{S}_z$ *do not anticommute* (unlike the Pauli matrices). For the same reason, the boundary-condition matching procedure of Ref. [59] is inadequate and non-generic for dealing with this system. Hence, our generic method is indispensable to explicitly derive the appearances of the Fermi arcs. We use the parametrisation $\psi_0^T = \begin{bmatrix} 1 & a_1 + i\, b_1 & a_2 + i\, b_2 \end{bmatrix}$ and consider a boundary at $x = 0$. Plugging it in Eq. (12) yields

$$\psi_0^\dagger\, \mathcal{S}_x\, \psi_0 = 0 \Rightarrow a_1 + a_2 = 0\,. \tag{20}$$

Employing the matrix equation, viz. Eq. (13), we get

$$\begin{aligned}
& i\,\kappa_r - \sqrt{2}\,(a_1 + i\,b_1)\,(E - k_z) = \kappa_i + i\,k_y\,, \quad -[a_1 + (1+i)a_2 + i\,b_1]\,(\kappa_i - i\,\kappa_r] + [i\,a_1 + (1-i)\,a_2 - b_1]\,k_y = \sqrt{2}\,E\,, \\
& \text{and } \sqrt{2}\,(1+i)\,a_2\,(E + k_z) = i\,(i\,\kappa_i + k_y + \kappa_r) \\
& \Rightarrow\; \kappa_i = \sqrt{2}\,a_1\,(k_z - E)\;, \quad \sqrt{2}\,b_1\,(k_z - E) + (\kappa_r - k_y) = 0\,, \quad (a_1 + a_2)\,\kappa_i + a_2\,[\kappa_r - k_y + b_1\,(k_y + \kappa_r)] = -\sqrt{2}\,E\,, \\
& (a_2 + b_1)\,\kappa_i = a_2\,(\kappa_r - k_y) + a_1\,(k_y + \kappa_r)\,, \quad \kappa_i = -\sqrt{2}\,a_2\,(E + k_z)\;, \quad \kappa_r = \sqrt{2}\,a_2\,(E + k_z) + k_y\,.
\end{aligned} \tag{21}$$

The solutions indeed tell us that there are two Fermi arcs characterised by (1) $E = \frac{2\sqrt{2}\,b_1\,k_y + 4\,k_z}{2 + b_1^2} - k_z$, $\kappa_r = \frac{(b_1^2 - 2)\,k_y + 2\sqrt{2}\,b_1\,k_z}{2 + b_1^2}$, $\kappa_i = 0$, $a_1 = 0$, $a_2 = -\,b_1^2/2$, $|b_1| > 0$, and $b_2 = 0$; and (2) $E = k_z$, $\kappa_r = -\,k_y$, $\kappa_i = 0$, $a_1 = 0$, $a_2 = 0$, $b_1 = 0$, and $b_2 = 0$. For the first arc, b_1 plays the role of a parameter and, hence, its shape changes as we vary b_1. The points on the SBZ where κ_r goes to zero are found to be $\{k_y, k_z\} = \frac{2\,\mu}{2 + b_1^2}\,\{b_1\,\sqrt{2},\, b_1^2 - 2\}$ (where $|b_1| > 0$) and $\{k_y, k_z\} = \{0,\, \mu\}$, respectively, for the two Fermi arcs.

For the case of two nodes separated along the k_z-direction (for example) by an amount k_w, which is possible when the nodes are not pinned at high-symmetry points for a given crystal structure, we can easily determine the nature of the Fermi arcs by the replacement $k_z \to (k_z^2 - k_w^2)$. Fig. 3(a) illustrates the Fermi arcs for $\mu = 0.5$, $k_w = 1$, and $b_1 = -1$. Since the nodes carry Chern numbers equalling ± 2, we observe two arcs emanating from each FS-projection.

D. Rarita-Schwinger-Weyl node in a chiral crystal

Here we focus on bands carrying pseudospin-3/2 quantum numbers crossing at fourfold-degenerate degenracy-points [cf. Fig. 1(a)], widely known as the Rarita-Schwinger-Weyl (RSW) nodes. They appear at the Γ-points of chiral crystals with appreciable SOC couplings [5, 12, 28, 42, 60], hosting a net BC-monopole of magnitude 4. The effective Hamiltonian, in the vicinity of an isotropic RSW node, takes the form of

$$\mathcal{H}(\boldsymbol{k}) = \mathbf{k}\cdot\boldsymbol{\mathcal{J}}\,. \tag{22}$$

Here, $\boldsymbol{\mathcal{J}} = \{\mathcal{J}_x,\, \mathcal{J}_y,\, \mathcal{J}_z\}$ represents the vector operator whose three components comprise the angular-momentum operators in the spin-3/2 representation of the SU(2) group. We choose the commonly-used representation with

$$\mathcal{J}_x = \begin{pmatrix} 0 & \frac{\sqrt{3}}{2} & 0 & 0 \\ \frac{\sqrt{3}}{2} & 0 & 1 & 0 \\ 0 & 1 & 0 & \frac{\sqrt{3}}{2} \\ 0 & 0 & \frac{\sqrt{3}}{2} & 0 \end{pmatrix}, \quad \mathcal{J}_y = \begin{pmatrix} 0 & \frac{-i\sqrt{3}}{2} & 0 & 0 \\ \frac{i\sqrt{3}}{2} & 0 & -i & 0 \\ 0 & i & 0 & \frac{-i\sqrt{3}}{2} \\ 0 & 0 & \frac{i\sqrt{3}}{2} & 0 \end{pmatrix}, \quad \mathcal{J}_z = \begin{pmatrix} \frac{3}{2} & 0 & 0 & 0 \\ 0 & \frac{1}{2} & 0 & 0 \\ 0 & 0 & -\frac{1}{2} & 0 \\ 0 & 0 & 0 & -\frac{3}{2} \end{pmatrix}. \tag{23}$$

Since the RSW node carries Chern number equalling 4, we must observe four arcs emanating from the FS-projections of the two nodes being cut by μ. For this case, just for the ease of calculations, we consider a boundary at $z = 0$ (just because the $\mathcal{J}$ matrix has fewer nonzero entries, leading to less cumbersome equations to be solved). Here again we note that, although this is a fourfold generalisation of the isotropic Weyl node, we cannot apply Witten's method since $\mathcal{J}_x$, $\mathcal{J}_y$, and $\mathcal{J}_z$ *do not anticommute* (unlike the Pauli matrices). Hence, we need to utilise our generic method to explicitly derive the equations of the Fermi arcs. We use the parametrisation $\psi_0^T = \begin{bmatrix} 1 & a_1 + i\,b_1 & a_2 + i\,b_2 & a_3 + i\,b_3 \end{bmatrix}$ because of the fourfold nature of the bands. Plugging it in Eq. (12) yields

$$\psi_0^\dagger\,\mathcal{J}_z\,\psi_0 = 0 \Rightarrow 3 - 3\,(a_3^2 + b_3^2) + a_1^2 + b_1^2 - (a_2^2 + b_2^2) = 0\,. \tag{24}$$

Employing the matrix equation, viz. Eq. (13), we get

$$\begin{aligned}
&2\,E = \sqrt{3}\,(a_1 + i\,b_1)\,(k_x - i\,k_y) - 3\,\kappa_i + 3\,i\,\kappa_r\,,\\
&(a_1 + i\,b_1)\,(2\,E + \kappa_i - i\,\kappa_r) = \left(2\,a_2 + 2\,i\,b_2 + \sqrt{3}\right) k_x + \left(2\,b_2 - 2\,i\,a_2 + i\,\sqrt{3}\right) k_y\,,\\
&(a_2 + i\,b_2)\,(2\,E - \kappa_i + i\,\kappa_r) = \sqrt{3}\,a_3\,(k_x - i\,k_y) + 2\,a_1\,(k_x + i\,k_y) + 2\,i\,b_1 k_x + i\,\sqrt{3}\,b_3\,k_x - 2\,b_1\,k_y + \sqrt{3}\,b_3\,k_y\,,\\
&\sqrt{3}\,(a_2 + i\,b_2)\,(k_x + i\,k_y) = (a_3 + i\,b_3)\,(2\,E - 3\,\kappa_i + 3\,i\,\kappa_r)\\
&\Rightarrow 2\,E = \sqrt{3}\,a_1\,k_x + \sqrt{3}\,b_1\,k_y - 3\,\kappa_i\,, \quad \sqrt{3}\,a_1\,k_y = \sqrt{3}\,b_1\,k_x + 3\,\kappa_r\,, \quad a_1\,(2\,E + \kappa_i) = \left(2\,a_2 + \sqrt{3}\right) k_x + 2\,b_2\,k_y - b_1\,\kappa_r\,,\\
&\quad 2\,a_2\,k_y = a_1\,\kappa_r - b_1\,(2\,E + \kappa_i) + 2\,b_2\,k_x + \sqrt{3}\,k_y\,, \quad 2\,b_1\,k_y = a_2\,(\kappa_i - 2\,E) + 2\,a_1\,k_x + \sqrt{3}\,a_3\,k_x + \sqrt{3}\,b_3\,k_y + b_2\,\kappa_r\,,\\
&\quad a_2\,\kappa_r = 2\,a_1\,k_y - \sqrt{3}\,a_3\,k_y + b_2\,(\kappa_i - 2\,E) + 2\,b_1\,k_x + \sqrt{3}\,b_3\,k_x\,, \quad 2\,a_3\,E = 3\,a_3\,\kappa_i + \sqrt{3}\,a_2\,k_x - \sqrt{3}\,b_2\,k_y + 3\,b_3\,\kappa_r\,,\\
&\quad 2\,b_3\,E = \sqrt{3}\,a_2\,k_y - 3\,a_3\,\kappa_r + 3\,b_3\,\kappa_i + \sqrt{3}\,b_2\,k_x\,.
\end{aligned} \tag{25}$$

The explicit solutions are long and cumbersome and can be parametrised in terms of one free parameter (which could be any of the $\{a_1,\, a_2,\, a_3,\, b_1,\, b_2,\, b_3\}$). Hence, we do not write those explicitly. Instead, we show the arcs in Fig. 3(b) for one single case by setting $\mu = 0.5$. The figure shows four Fermi arcs, in total, emanating outside the projection of the outer FS.

E. Double-Weyl semimetal

Double-Weyl nodes can be found in materials like $HgCr_2Se_4$ [61] and $SrSi_2$ [62, 63]), which exhibits a hybrid of linear dispersion (chosen to be the k_z-axis) and quadratic dispersion (in the $k_x k_y$-plane). In the vicinity of such a nodal point, the low-energy effective continuum Hamiltonian is given by [4, 18, 23, 27]

$$H_{dW} = \boldsymbol{d}\cdot\boldsymbol{\sigma}\,, \text{ where } \boldsymbol{d} \equiv \{d_x,\, d_y,\, d_z\} = \left\{\frac{k_x^2 - k_y^2}{k_0},\, \frac{2\,k_x\,k_y}{k_0},\, k_z\right\}, \tag{26}$$

where k_0 is a material-dependent parameter. For simplicity, we assume the momenta to be scaled such that k_0 can be set to 1. Plugging in the parametrisation of $\psi_0^T = \begin{bmatrix} 1 & a_1 + i\,b_1 \end{bmatrix}$ in Eq. (12) leads to

$$\kappa_i\,\psi_0^\dagger\,\sigma_x\,\psi_0 = k_y\,\psi_0^\dagger\,\sigma_y\,\psi_0 \Rightarrow \kappa_i = \frac{b_1}{a_1}\,k_y\,. \tag{27}$$

Additionally, the two components of the matrix of Eq. (13) provide us with the following:

$$\begin{aligned}
&E = k_z - (a_1 + i\,b_1)\,(i\,\kappa_i - k_y + \kappa_r)^2 \text{ and } (a_1 + i\,b_1)\,(E + k_z) + (i\,\kappa_i + k_y + \kappa_r)^2 = 0\\
&\Rightarrow E = k_z - a_1\left(-2\left(p^2 + 1\right) k_y \kappa_r + \left(p^2 + 1\right) k_y^2 + \kappa_r^2\right)\,.
\end{aligned} \tag{28}$$

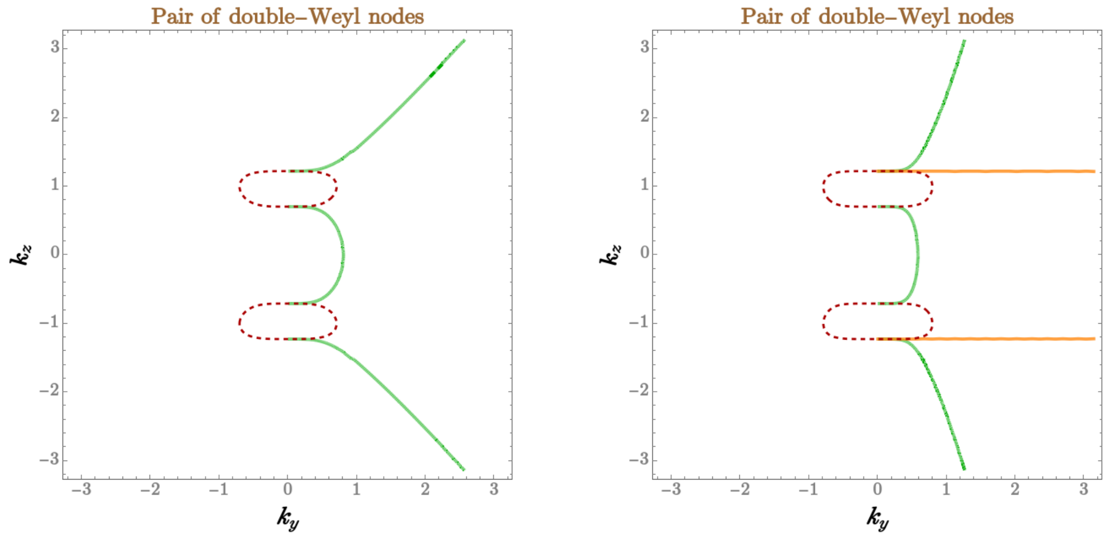

(a)

(b)

FIG. 4. The Fermi arcs represent modes with $E = \mu$, where $\mu = 0.5$ and $k_w = 1$. (a) A pair of double-Weyl nodes source two arcs from the perimeter of each FS- projection. Here, $t = \pi/6$ and $s = 1$. (b) A pair of triple-Weyl nodes: source two arcs from the perimeter of each FS- projection. Here, $t = 0$ and $s = 1$.

The solutions are found easily after parametrising $a_1 = a\cos t$ and $b_1 = a\sin t$: $E = \frac{\sqrt{k_z^2\cos^2 t - 4\,k_y^4\tan^2 t}}{\cos t}$, $\kappa_r = \frac{s\,k_y}{\cos(t)}$, , where $a = s\,\frac{k_z\,\cos t - \sqrt{k_z^2\cos^2 t - 4\,k_y^4\tan^2 t}}{2\,k_y^2\left(1+\frac{1}{\cos t}\right)}$ and $s = \pm 1$. Thus, t serves an undetermined parameter, producing curves of varying shapes. The points on the SBZ where κ_r goes to zero are found to be $\{k_y, k_z\} = \{0,\, \pm\mu\}$.

For the case of two nodes separated along the k_z-direction by an amount k_w, we can easily determine the nature of the Fermi arcs by the replacement $k_z \to (k_z^2 - k_w^2)$. Fig. 4(a) illustrates the Fermi arcs for $\mu = 0.5$, $k_w = 1$, and $t = \pi/6$. Since the nodes carry Chern numbers equalling ± 2, we observe two arcs emanating from the perimeter of each FS-projection.

F. Triple-Weyl semimetal

Analogous to the double-Weyl nodes, there exist triple-Weyl nodes (in materials like transition-metal monochalcogenides [64]) from which bands with anisotropic dispersion emerge. The triple-Weyl case comprises a hybrid of linear dispersion (chosen to be the k_z-axis) and quadratic dispersion (in the $k_x k_y$-plane). In the vicinity of such a nodal point, the low-energy effective continuum Hamiltonian is given by [4, 18, 27]

$$H_{tW} = \boldsymbol{d}\cdot\boldsymbol{\sigma}\,, \text{ where } \boldsymbol{d} \equiv \{d_x,\, d_y,\, d_z\} = \left\{ \frac{k_x^3 - 3\,k_x\,k_y^2}{k_0^2},\, \frac{3\,k_x^2\,k_y - k_y^3}{k_0^2},\, k_z \right\}, \tag{29}$$

where k_0 is a material-dependent parameter. Again, for simplicity, we set k_0 to 1. Plugging in the parametrisation of $\psi_0^T = \begin{bmatrix} 1 & a_1 + i\,b_1 \end{bmatrix}$ in Eq. (12) leads to

$$\left[3\,k_y^2 + (\kappa_r - i\,\kappa_i)^2 + (\kappa_r + i\,\kappa_i)^2 - \kappa_r^2 - \kappa_i^2\right]\psi_0^\dagger\,\sigma_x\,\psi_0 + 6\,\kappa_i k_y\,\psi_0^\dagger\,\sigma_y\,\psi_0 = 0 \Rightarrow a_1\left(\kappa_r^2 - 3\,\kappa_i^2 + 3\,k_y^2\right) + 6\,b_1\kappa_i\,k_y = 0\,. \tag{30}$$

Additionally, the two components of the matrix of Eq. (13) provide us with the following:

$$\begin{aligned} & E = k_z - (a_1 + i\,b_1)\,(\kappa_i + i\,k_y - i\,\kappa_r)^3 \text{ and } i\,a_1\,(e + k_z) = b_1\,(E + k_z) + (i\,\kappa_i + k_y + \kappa_r)^3 \\ & \Rightarrow E = k_z - a_1\,\kappa_i\left[\kappa_i^2 - 3\,(k_y - \kappa_r)^2\right] - b_1\,(k_y - \kappa_r)\left[(k_y - \kappa_r)^2 - 3\,\kappa_i^2\right], \quad b_1\,(E + k_z) = (k_y + \kappa_r)\left[3\,\kappa_i^2 - (k_y + \kappa_r)^2\right], \\ & a_1\,(k_y - \kappa_r)\left[(k_y - \kappa_r)^2 - 3\,\kappa_i^2\right] = b_1\,\kappa_i\left[\kappa_i^2 - 3\,(k_y - \kappa_r)^2\right], \quad \kappa_i\left[3\,(k_y + \kappa_r)^2 - \kappa_i^2\right] = a_1\,(E + k_z)\,. \end{aligned} \tag{31}$$

Finding exact analytical solutions is cumbersome because of the cubit roots involved. Instead, we parametrise $a_1 = a\cos t$ and $b_1 = \sin t$, and we show below the solutions for $t = 0$: (1) $E = k_z$, $\kappa_r = \pm\,k_y$, $\kappa_i = 0$, and $a = 0$; (2) $E = \frac{1}{3}\sqrt{9\,k_z^2 - \frac{512\,k_y^6}{3}}$, $\kappa_r = s\,k_y$, $\kappa^2 = \tilde{s}\,\frac{2\,k_y}{\sqrt{3}}$, and $a = s\,\tilde{s}\,\frac{3\sqrt{3}\,k_z - \sqrt{27\,k_z^2 - 512\,k_y^6}}{64\,k_y^3}$, where $(s, \tilde{s}) = \pm 1$. The points on the SBZ, where κ_r for the three arcs goes to zero, are found to be $\{k_y, k_z\} = \{0,\, \pm\mu\}$.

For the case of two nodes separated along the k_z-direction by an amount k_w, we can easily determine the nature of the Fermi arcs by the replacement $k_z \to (k_z^2 - k_w^2)$. Fig. 4(b) illustrates the Fermi arcs for $\mu = 0.5$, $k_w = 1$, and $s = 1$ (the value of $\tilde{s}$ does not matter) for the solution detailed above. Since the nodes carry Chern numbers equalling ± 3, we observe three arcs emanating from the perimeter of each FS-projection.

G. Berry-dipole in a two-band model

In a specific two-band model, the low-energy effective Hamiltonian in the vicinity of a single node harbouring a Berry-dipole [cf. Fig. 1(b)] is captured by [14]

$$H_{bd}(k_x, k_y, k_z) = 2\, v\, v_z\, q_z\, (q_x\, \sigma_x + q_y\, \sigma_y) + \left[v^2 \left(q_x^2 + q_y^2\right) - q_z^2\right] \sigma_z \,. \tag{32}$$

Being an ideal dipole, this node carries vanishing BC-monopole charge. As such, one might think that there might be no Fermi arcs emerging on the SBZ. However, it turns out Fermi arcs do arise as surface states (on solving systematically using the generic method outlined in Sec. II B), representing edge states on 2d slices carrying opposite Chern numbers.

Since this is a two-band model, we again use $\psi_0^T = \begin{bmatrix} 1 & a_1 + i\, b_1 \end{bmatrix}$. Plugging it in Eq. (12) yields

$$v_p^2\, \kappa_i\, \psi_0^\dagger\, \sigma_z\, \psi_0 + v_p\, k_z\, \psi_0^\dagger\, \sigma_x\, \psi_0 = 0 \Rightarrow 2\, a_1\, k_z - v_p \left(a_1^2 + b_1^2 - 1\right) \kappa_i = 0. \tag{33}$$

Next, the two components of the matrix of Eq. (13) take the forms of

$$\begin{aligned}
&E = 2\,(b_1 - i\, a_1)\, v_p\, v_z\, k_z\, (k_y - \kappa_r - \kappa_i) + v_p^2 \left[k_y^2 - (\kappa_i + \kappa_r)^2\right] - v_z^2\, k_z^2 \\
&\text{and } \ (a_1 + i\, b_1) \left[v_z^2\, k_z^2 - v_p^2\, k_y^2 + v_p^2\, (\kappa_i + \kappa_r)^2 - E\right] + 2\, i\, k_z\, v_p\, v_z\, (k_y + \kappa_r + \kappa_i) = 0 \\
\Rightarrow\ & E = -2\, b_1\, v_p\, v_z\, k_z\, (\kappa_r + \kappa_i) + 2\, b_1\, v_p\, v_z\, k_y\, k_z - v_p^2\, (\kappa_i + \kappa_r)^2 + v_p^2\, k_y^2 - v_z^2\, k_z^2\,, \quad a_1\, k_z\, (\kappa_r + \kappa_i - k_y) = 0\,, \\
& a_1 \left(v_p^2\, (\kappa_r + \kappa_i)^2 - v_p^2\, k_y^2 + v_z^2\, k_z^2 - E\right) = 0\,, \quad b_1 \left[v_p^2\, (\kappa_r + \kappa_i)^2 - v_p^2\, k_y^2 + v_z^2\, k_z^2 - E\right] + 2\, v_p\, v_z\, k_z\, (\kappa_r + \kappa_i + k_y) = 0\,.
\end{aligned} \tag{34}$$

We obtain the solutions as $E = \frac{k_z\, v_z}{b_1^2} \left[2\, b_1\, v_p\, k_y + \left(b_1^2 - 1\right) k_z\, v_z\right]$, $\kappa_r = k_y - \frac{k_z v_z}{b_1 v_p}$, $\kappa_i = 0$, and $a_1 = 0$. The points on the SBZ where κ_r goes to zero (and the arc becomes tangential to the projection of the FS) are found to be $\{k_y, k_z\} = \pm \sqrt{\frac{\mu}{1+b_1^2}}\, \{\frac{1}{v_p},\, \frac{b_1}{v_z}\}$, denoting antipodal points on a FS-projection. In fact, these tangents are anti-parallel, being proportional to $\pm \frac{2\, v_p\, \sqrt{\mu}}{\sqrt{1+b_1^2}} \{1,\, b_1\}$.

If the BZ contains two BC-dipole nodes, separated along the k_z-direction by an amount k_w, the answers are obtained by the replacement $k_z \to (k_z^2 - k_w^2)$. Fig. 5(a) shows the resulting Fermi arcs for a particular choice of the parameter-values. Evidently, two Fermi arcs graze past each FS-projection.

H. Berry-dipole in a three-band model

In Ref. [15], massless multifold Hopf semimetals (MMHSs) have been introduced which host BC-dipoles at nodes where linearly-dispersing bands cross. We consider the simplest case with threefold-degenerate node, captured by the effective continuum Hamiltonian [15, 16],

$$H_H = k_x\, \lambda_1 + k_y\, \lambda_2 + k_z\, \lambda_5\,, \tag{35}$$

where

$$\lambda_1 = \begin{bmatrix} 0 & 1 & 0 \\ 1 & 0 & 0 \\ 0 & 0 & 0 \end{bmatrix}, \quad \lambda_2 = \begin{bmatrix} 0 & -i & 0 \\ i & 0 & 0 \\ 0 & 0 & 0 \end{bmatrix}, \quad \lambda_5 = \begin{bmatrix} 0 & 0 & -i \\ 0 & 0 & 0 \\ i & 0 & 0 \end{bmatrix}. \tag{36}$$

For this 3-band model, we use the parametrisation $\psi_0^T = \begin{bmatrix} 1 & a_1 + i\, b_1 & a_2 + i\, b_2 \end{bmatrix}$. For a boundary at $x = 0$, plugging it in Eq. (12) yields

$$\psi_0^\dagger\, \lambda_1\, \psi_0 = 0 \Rightarrow a_1 = 0\,. \tag{37}$$

Employing the matrix equation, viz. Eq. (13), we get

$$\begin{aligned}
&(b_2 - i\, a_2)\, k_z + b_1\, (-i\kappa_2 + k_y - \kappa_r) = E \text{ and } k_y + \kappa_r + i\, \kappa_i = b_1\, E \\
&b_1\, (k_y - \kappa_r) + b_2\, k_z = E\,, \quad a_2\, k_z + b_1\, \kappa_i = 0\,, \quad \kappa_i = 0\,, \quad b_1\, E = k_y + \kappa_r\,, \quad a_2\, E = 0\,, \quad b_2\, E = k_z\,.
\end{aligned} \tag{38}$$

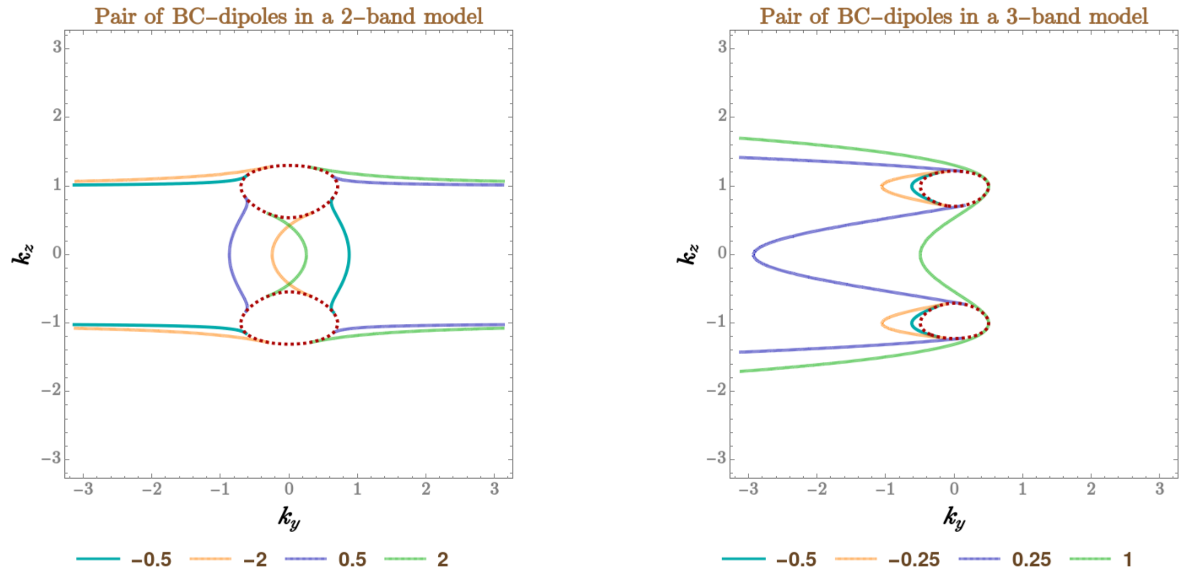

(a) (b)

FIG. 5. The Fermi arcs represent modes with $E = \mu$, where $\mu = 0.5$ and $k_w = 1$. The dashed red closed contours represent the projections of the bulk FSs on the $k_y k_z$-plane. Each arc corresponds to a distinct value of b_1, colour-coded as shown in the plot-legends. A pair of nodes carrying ideal BC-dipoles using the model in (a) Eq. (32), using $v_p = v_z = 1$; (b) Eq. (35). In each case, Fermi arcs graze through each FS-projection at two distinct points, meeting tangentially along a FS-projection.

The solutions turn out to be $E = \frac{b_1\, k_y + \sqrt{b_1^2 \left(k_y^2+k_z^2\right)+k_z^2}}{1+b_1^2}$, $\kappa_r = \frac{k_z^2 + b_1 \sqrt{b_1^2\left(k_y^2+k_z^2\right)} - k_y}{1+b_1^2}$, $\kappa_i = 0$, $a_2 = 0$, and $b_2 = \frac{\sqrt{b_1^2\left(k_y^2+k_z^2\right)+k_z^2} - b_1 k_y}{k_z}$. The points on the SBZ where κ_r goes to zero (and the arc becomes tangential to the projection of the FS) are found to be $\{k_y, k_z\} = \mu\,\{b_1, \pm\sqrt{1-b_1^2}\}$. This also tells us that the parameter b_1 is constrained to obey $|b_1| \leq 1$. The corresponding tangents are proportional to $\{b_1, \pm\sqrt{1-b_1^2}\}$ and, hence, are related by flipping the signs of their k_z-components.

If the BZ contains two BC-dipole nodes, separated along the k_z-direction by an amount k_w, the answers are obtained by the replacement $k_z \to (k_z^2 - k_w^2)$. Fig. 5(b) demonstrates the nature of the Fermi arcs for some distinct values of b_1. Depending on the value of b_1, either two separate Fermi arcs graze past each FS-projection, or the same Fermi arc folds back and rejoins the same FS-projection.

I. Quadruple-Weyl node with monopole-charge 4

A quadruple-Weyl node (QWN) with twofold degeneracy carries BC-monopole charge of magnitude 4 [65–68] and can exist only in spinless systems at specific time-reversal symmetric points. Thus, they can appear in electronic bandstructures of materials with negligible SOC-couplings or in the phonon spectra of artificial crystals (such as photonic crystals), all of which can be treated as spinless systems. Let us take the lattice model of Ref. [68], where two nodes of opposite chiralities emerge at the Γ- and R-points. For the node sitting at the Γ-point can be described by the Hamiltonian,

$$H_{qW} = \boldsymbol{d}\cdot\boldsymbol{\sigma}\,, \text{ where } \boldsymbol{d} \equiv \{d_x,\, d_y,\, d_z\} = \left\{ \frac{v\left(k_x^2 - k_y^2\right)}{2},\, \frac{\left(k_x^2 + k_y^2 - 2\,k_z^2\right)}{2},\, v\, k_x\, k_y\, k_z \right\}. \tag{39}$$

Here we fix v to be positive. The energy eigenvalues are given by $\pm\sqrt{v^2\left[2\,k_x^2\,k_y^2\,(2\,k_z^2-1)+k_x^4+k_y^4\right]+\left(k_x^2+k_y^2-2\,k_z^2\right)^2}/2$. Clearly, the dispersion of the bands are anisotropic, with a cubic dispersion along the (111) direction and quadratic dispersion along any other direction. Here, we expect 4 Fermi arcs to emanate from the nodal point [44], which we will derive explicitly by considering a boundary at $x = 0$.

On using $\psi_0^T = \begin{bmatrix} 1 & a_1 + i\,b_1 \end{bmatrix}$, Eq. (12) yields

$$\kappa_i\left(v\,\psi_0^\dagger\,\sigma_x\,\psi_0 + \psi_0^\dagger\,\sigma_y\,\psi_0\right) + v\,k_y\,k_z\,\psi_0^\dagger\,\sigma_z\,\psi_0 = 0 \Rightarrow 2\,\kappa_i\,(a_1\,v + b_1) = v\left(a_1^2 + b_1^2 - 1\right)k_y\,k_z\,. \tag{40}$$

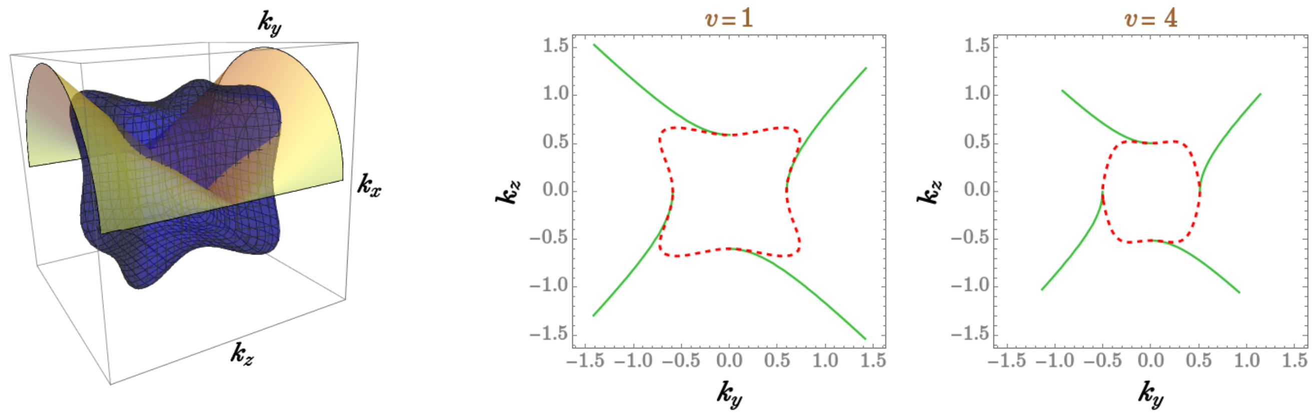

(a) (b)

FIG. 6. (a) The FS-projection is obtained by cutting the 3d FS with the yellow-coloured 2d surface, captured by Eq. (42). Here, $\mu = 0.25$ and $v = 1$. (b) The Fermi arcs represent modes with $E = \mu$, where $\mu = 0.25$. The dashed red closed contour represents the projection of the bulk FS on the $k_y k_z$-plane.

Employing the matrix equation of Eq. (13), we get

$$
\begin{aligned}
& a_1 \left[(v-i)\,(\kappa_i - i\,\kappa_r)^2 - (v+i)\,k_y^2 + 2\,i\,k_z^2\right] + b_1 \left[(1+i\,v)\,(\kappa_i - i\,\kappa_r)^2 + (1-i\,v)\,k_y^2 - 2\,k_z^2\right] = 2\,E + 2\,v\,k_y\,k_z\,(\kappa_i - i\,\kappa_r) \\
& \text{and } a_1\,E = a_1\,v\,k_y\,k_z\,(\kappa_i - i\,\kappa_r) - i\,b_1\,E + b_1\,v\,k_y\,k_z\,(\kappa_r + i\,\kappa_i) + \frac{v+i}{2}\,(\kappa_i - i\,\kappa_r)^2 - \frac{(v-i)\,k_y^2}{2} - i\,k_z^2 \\
& \Rightarrow 2\,E + 2\,v\,\kappa_i\,k_y\,k_z = b_1\left(\kappa_i^2 + 2\,v\,\kappa_i\,\kappa_r + k_y^2 - 2\,k_z^2 - \kappa_r^2\right) - a_1\left[2\,\kappa_i\,\kappa_r + v\left(\kappa_r^2 - \kappa_i^2\right) + v\,k_y^2\right], \\
& \qquad a_1\left(\kappa_i^2 + 2\,v\,\kappa_i\,\kappa_r + k_y^2 - 2\,k_z^2 - \kappa_r^2\right) = -\,b_1\left(2\,\kappa_i\,\kappa_r - v\,\kappa_i^2 + v\,k_y^2 + v\,\kappa_r^2\right) + 2\,v\,k_y\,k_z\,\kappa_r\,, \\
& \qquad 2\,a_1\,E = 2\,a_1\,v\,\kappa_i\,k_y\,k_z + 2\,\kappa_r\,(b_1\,v\,k_y\,k_z + \kappa_i) + v\,\kappa_i^2 - v\,k_y^2 - v\,\kappa_r^2\,, \\
& \qquad 2\,b_1\,E = -\,2\,v\,\kappa_r\,(a_1\,k_y\,k_z + \kappa_i) + 2\,b_1\,v\,\kappa_i\,k_y\,k_z + \kappa_i^2 + k_y^2 - 2\,k_z^2 - \kappa_r^2\,.
\end{aligned}
\tag{41}
$$

The admissible solutions for $\mu \geq 0$ are (1) $E = -\frac{v\left(k_y^2 - k_z^2\right)}{\sqrt{1+v^2}}$, $\kappa_r = -\,k_y\,k_z$, $\kappa_i = \pm\sqrt{\frac{2\,k_z^2 - k_y^2\left[v^2\,(k_z^2-1)+1\right]}{1+v^2}}$, $a_1 = \frac{1}{\sqrt{v^2+1}}$, and $b_1 = \frac{-\,v}{\sqrt{v^2+1}}$; and (2) $E = \frac{v\left(k_y^2 - k_z^2\right)}{\sqrt{1+v^2}}$, $\kappa_r = k_y\,k_z$, $\kappa_i = \pm\sqrt{\frac{2\,k_z^2 - k_y^2\left[v^2\,(k_z^2-1)+1\right]}{1+v^2}}$, $a_1 = \frac{-\,1}{\sqrt{v^2+1}}$, and $b_1 = \frac{v}{\sqrt{v^2+1}}$.

Unlike the cases discussed so far, the projection of the FS on the $x = 0$ boundary is not obtained by setting $k_x = 0$. Instead, it is given by the values $k_x = \pm\frac{\sqrt{2\,k_z^2 - 2\,v^2\,k_y^2\,k_z^2 + (v^2-1)\,k_y^2}}{\sqrt{1+v^2}}$, which leads to the closed curve (lying in the $k_y k_z$-plane) defined by

$$
v\,\sqrt{\frac{k_z^4 - k_y^4\,(k_z^2-1)\,(1+v^2\,k_z^2) + 2\,k_y^2\,k_z^2\,(k_z^2-1)}{1+v^2}} = \mu\,. \tag{42}
$$

The case of $v = 1$ and $\mu = 0.25$ is illustrated in Fig. 6(a). Keeping this in mind, the points on the SBZ where κ_r goes to zero, becoming tangential to the FS-projection, are found to be $\{k_y, k_z\} = \left\{0, \pm\frac{\sqrt{\mu}\,\sqrt[4]{1+v^2}}{\sqrt{v}}\right\}$ and $\{k_y, k_z\} = \left\{\pm\frac{\sqrt{\mu}\,\sqrt[4]{1+v^2}}{\sqrt{v}}, 0\right\}$, respectively. Therefore, for different values of, we get Fermi arcs of distinct shapes. The tangents to the FS-projection, where the arcs meet the bulk states, are proportional to $\left\{0, \pm\frac{4\,\mu^{3/2}\,\sqrt{v}}{\sqrt[4]{1+v^2}}\right\}$ and $\left\{\pm\frac{4\,\mu^{3/2}\,\sqrt{v}}{\sqrt[4]{1+v^2}}, 0\right\}$. Fig. 6(b) illustrates the arcs for $\mu = 0.25$ and two values of v. It might seem that the arcs end in thin air, but in actual lattice calculations, they will be found to end on some other nodal point or continue as arcs connecting with those ending on the conjugate QWN-projections located at the R-point. The effective Hamiltonian in Eq. (39), correct only in the vicinity of the node, of course cannot capture such global details.

IV. SUMMARY AND OUTLOOK

Our derivations for the nature of surface states in 3d semimetals provide an exhaustive analysis of generic boundary conditions. The main line of argument hinges on the presevation of self-adjointness (i.e., Hermiticity) of the effective Hamiltonian of the corresponding surface, which must host eigenstates that decay exponentially as we move away from the boundary with the topological material. On the side of the material itself, the states must merge with the eigenstates (of the bulk Hamiltonian) representing the 3d bulk states. Through explicit examples, we have shown how the number of Fermi arcs, arising in the SBZ, gives us a clear signature of the net Chern number at a given nodal point, conforming to the well-established notion of bulk-boundary correspondence. However exotic the bandstructure might be, our formalism will work in all generic cases. In the future, we plan to investigate the dynamics of the surface states, for example when a magnetic field is applied, when we can observe quantum oscillations [1, 69].

---

[1] A. A. Burkov and L. Balents, Weyl semimetal in a topological insulator multilayer, Phys. Rev. Lett. **107**, 127205 (2011); P. Hosur, Friedel oscillations due to Fermi arcs in Weyl semimetals, Phys. Rev. B **86**, 195102 (2012).

[2] N. P. Armitage, E. J. Mele, and A. Vishwanath, Weyl and Dirac semimetals in three-dimensional solids, Rev. Mod. Phys. **90**, 015001 (2018); P. Hosur and X. Qi, Recent developments in transport phenomena in Weyl semimetals, Comptes Rendus Physique **14**, 857 (2013); B. Yan and C. Felser, Topological materials: Weyl semimetals, Annual Rev. of Condensed Matter Phys. **8**, 337 (2017).

[3] I. Mandal and K. Saha, Thermoelectric response in nodal-point semimetals, Ann. Phys. (Berlin) **536**, 2400016 (2024).

[4] B. Bradlyn, J. Cano, Z. Wang, M. G. Vergniory, C. Felser, R. J. Cava, and B. A. Bernevig, Beyond Dirac and Weyl fermions: Unconventional quasiparticles in conventional crystals, Science **353** (2016); C. Fang, M. J. Gilbert, X. Dai, and B. A. Bernevig, Multi-Weyl topological semimetals stabilized by point group symmetry, Phys. Rev. Lett. **108**, 266802 (2012).

[5] F. Flicker, F. de Juan, B. Bradlyn, T. Morimoto, M. G. Vergniory, and A. G. Grushin, Chiral optical response of multifold fermions, Phys. Rev. B **98**, 155145 (2018).

[6] F. Balduini, A. Molinari, L. Rocchino, V. Hasse, C. Felser, M. Sousa, C. Zota, H. Schmid, A. G. Grushin, and B. Gotsmann, Intrinsic negative magnetoresistance from the chiral anomaly of multifold fermions, Nature Communications **15**, 6526 (2024).

[7] L. Liang and Y. Yu, Semimetal with both Rarita-Schwinger-Weyl and Weyl excitations, Phys. Rev. B **93**, 045113 (2016).

[8] H. Isobe and L. Fu, Quantum critical points of $j = \frac{3}{2}$ Dirac electrons in antiperovskite topological crystalline insulators, Phys. Rev. B **93**, 241113 (2016).

[9] P. Tang, Q. Zhou, and S.-C. Zhang, Multiple types of topological fermions in transition metal silicides, Phys. Rev. Lett. **119**, 206402 (2017).

[10] J.-Z. Ma, Q.-S. Wu, M. Song, S.-N. Zhang, E. Guedes, S. Ekahana, M. Krivenkov, M. Yao, S.-Y. Gao, W.-H. Fan, *et al.*, Observation of a singular Weyl point surrounded by charged nodal walls in PtGa, Nature Communications **12**, 3994 (2021).

[11] Y. Shen, Y. Jin, Y. Ge, M. Chen, and Z. Zhu, Chiral topological metals with multiple types of quasiparticle fermions and large spin Hall effect in the SrGePt family materials, Phys. Rev. B **108**, 035428 (2023).

[12] R. Ghosh, F. Haidar, and I. Mandal, Linear response in planar Hall and thermal Hall setups for Rarita-Schwinger-Weyl semimetals, Phys. Rev. B **110**, 245113 (2024); I. Mandal, S. Saha, and R. Ghosh, Signatures of topology in generic transport measurements for Rarita-Schwinger-Weyl semimetals, Solid State Communications **397**, 115799 (2025); I. Mandal, Distinguishing features of longitudinal magnetoconductivity for a Rarita-Schwinger-Weyl node, arXiv e-prints (2025), arXiv:2506.12380 [cond-mat.mes-hall].

[13] D. Xiao, M.-C. Chang, and Q. Niu, Berry phase effects on electronic properties, Rev. Mod. Phys. **82**, 1959 (2010); G. Sundaram and Q. Niu, Wave-packet dynamics in slowly perturbed crystals: Gradient corrections and Berry-phase effects, Phys. Rev. B **59**, 14915 (1999); A. Graf and F. Piéchon, Berry curvature and quantum metric in N-band systems: An eigenprojector approach, Phys. Rev. B **104**, 085114 (2021).

[14] Z.-Y. Zhuang, C. Zhang, X.-J. Wang, and Z. Yan, Berry-dipole semimetals, Phys. Rev. B **110**, L121122 (2024).

[15] A. Graf and F. Piéchon, Massless multifold Hopf semimetals, Phys. Rev. B **108**, 115105 (2023).

[16] T. Habe, Optical conductivity of the threefold Hopf semimetal, Phys. Rev. B **106**, 205204 (2022); S. Ahn, Magneto-optical conductivity of threefold Hopf semimetals, Journal of the Korean Physical Society **84**, 59 (2024).

[17] A. Knoll, C. Timm, and T. Meng, Negative longitudinal magnetoconductance at weak fields in Weyl semimetals, Phys. Rev. B **101**, 201402 (2020).

[18] R. Ghosh and I. Mandal, Electric and thermoelectric response for Weyl and multi-Weyl semimetals in planar Hall configurations including the effects of strain, Physica E: Low-dimensional Systems and Nanostructures **159**, 115914 (2024); Direction-dependent conductivity in planar Hall set-ups with tilted Weyl/multi-Weyl semimetals, Journal of Physics: Condensed Matter **36**, 275501 (2024); L. Medel, R. Ghosh, A. Martín-Ruiz, and I. Mandal, Electric, thermal, and thermoelectric magnetoconductivity for Weyl/multi-Weyl semimetals in planar Hall set-ups induced by the combined effects of topology and strain, Scientific Reports **14**, 21390 (2024); I. Mandal, Anisotropic conductivity for the type-I and type-II phases of Weyl/multi-Weyl semimetals in planar Hall set-ups, Annals of Physics **482**, 170181 (2025); I. Mandal, Effects of time-periodic drive in the linear response for planar-Hall set-ups with Weyl and multi-Weyl semimetals, arXiv e-prints (2025), arXiv:2503.14406 [cond-mat.mes-hall].

[19] F. D. M. Haldane, Berry curvature on the Fermi surface: Anomalous Hall effect as a topological Fermi-liquid property, Phys. Rev. Lett. **93**, 206602 (2004).

[20] P. Goswami and S. Tewari, Axionic field theory of $(3+1)$-dimensional Weyl semimetals, Phys. Rev. B **88**, 245107 (2013).

[21] A. A. Burkov, Anomalous Hall effect in Weyl metals, Phys. Rev. Lett. **113**, 187202 (2014).

[22] S.-B. Zhang, H.-Z. Lu, and S.-Q. Shen, Linear magnetoconductivity in an intrinsic topological Weyl semimetal, New Journal of Phys. **18**, 053039 (2016).

[23] Q. Chen and G. A. Fiete, Thermoelectric transport in double-Weyl semimetals, Phys. Rev. B **93**, 155125 (2016).

[24] S. Nandy, G. Sharma, A. Taraphder, and S. Tewari, Chiral anomaly as the origin of the planar Hall effect in Weyl semimetals, Phys. Rev. Lett. **119**, 176804 (2017); S. Nandy, A. Taraphder, and S. Tewari, Berry phase theory of planar Hall effect in topological insulators, Scientific Reports **8**, 14983 (2018).

[25] K. Das and A. Agarwal, Linear magnetochiral transport in tilted type-I and type-II Weyl semimetals, Phys. Rev. B **99**, 085405 (2019).
[26] O. Pal, B. Dey, and T. K. Ghosh, Berry curvature induced magnetotransport in 3D noncentrosymmetric metals, Journal of Phys.: Condensed Matter **34**, 025702 (2022).
[27] L. X. Fu and C. M. Wang, Thermoelectric transport of multi-Weyl semimetals in the quantum limit, Phys. Rev. B **105**, 035201 (2022).
[28] M. Stålhammar, J. Larana-Aragon, J. Knolle, and E. J. Bergholtz, Magneto-optical conductivity in generic Weyl semimetals, Phys. Rev. B **102**, 235134 (2020); S. Yadav, S. Sekh, and I. Mandal, Magneto-optical conductivity in the type-I and type-II phases of Weyl/multi-Weyl semimetals, Physica B: Condensed Matter **656**, 414765 (2023); I. Mandal, Chiral anomaly and internode scatterings in multifold semimetals, Phys. Rev. B **111**, 165116 (2025).
[29] F. Haidar and I. Mandal, Reflections of topological properties in the planar-Hall response for semimetals carrying pseudospin-1 quantum numbers, Annals of Physics **478**, 170010 (2025); I. Mandal, Longitudinal magnetoconductivity in chiral multifold semimetals exemplified by pseudospin-1 nodal points, arXiv e-prints (2025), arXiv:2505.19636 [cond-mat.mes-hall].
[30] F. H. Rather, F. Haidar, M. Jaffar A., and I. Mandal, Direction-dependent linear response for gapped nodal-line semimetals in planar-Hall configurations, arXiv e-prints (2025), arXiv:2503.10712 [cond-mat.mes-hall].
[31] I. Mandal, Disentangling contributions to longitudinal magnetoconductivity for Kramers-Weyl nodes, arXiv e-prints (2025), arXiv:2506.07913 [cond-mat.mes-hall].
[32] M. Papaj and L. Fu, Magnus Hall effect, Phys. Rev. Lett. **123**, 216802 (2019); D. Mandal, K. Das, and A. Agarwal, Magnus Nernst and thermal Hall effect, Phys. Rev. B **102**, 205414 (2020); S. Sekh and I. Mandal, Magnus Hall effect in three-dimensional topological semimetals, Eur. Phys. J. Plus **137**, 736 (2022).
[33] S. Sekh and I. Mandal, Circular dichroism as a probe for topology in three-dimensional semimetals, Phys. Rev. B **105**, 235403 (2022); I. Mandal, Signatures of two- and three-dimensional semimetals from circular dichroism, International Journal of Modern Physics B **38**, 2450216 (2024).
[34] J. E. Moore, Optical properties of Weyl semimetals, National Science Rev. **6**, 206 (2018).
[35] C. Guo, V. S. Asadchy, B. Zhao, and S. Fan, Light control with Weyl semimetals, eLight **3**, 2 (2023).
[36] A. Avdoshkin, V. Kozii, and J. E. Moore, Interactions remove the quantization of the chiral photocurrent at Weyl points, Phys. Rev. Lett. **124**, 196603 (2020); I. Mandal, Effect of interactions on the quantization of the chiral photocurrent for double-Weyl semimetals, Symmetry **12** (2020).
[37] S.-Y. Xu, I. Belopolski, N. Alidoust, M. Neupane, G. Bian, C. Zhang, R. Sankar, G. Chang, Z. Yuan, C.-C. Lee, S.-M. Huang, H. Zheng, J. Ma, D. S. Sanchez, B. Wang, A. Bansil, F. Chou, P. P. Shibayev, H. Lin, S. Jia, and M. Z. Hasan, Discovery of a Weyl fermion semimetal and topological Fermi arcs, Science **349**, 613 (2015).
[38] B. Q. Lv, H. M. Weng, B. B. Fu, X. P. Wang, H. Miao, J. Ma, P. Richard, X. C. Huang, L. X. Zhao, G. F. Chen, Z. Fang, X. Dai, T. Qian, and H. Ding, Experimental discovery of Weyl semimetal TaAs, Phys. Rev. X **5**, 031013 (2015).
[39] D. S. Sanchez, I. Belopolski, T. A. Cochran, X. Xu, J.-X. Yin, G. Chang, W. Xie, K. Manna, V. Süß, C.-Y. Huang, N. Alidoust, D. Multer, S. S. Zhang, N. Shumiya, X. Wang, G.-Q. Wang, T.-R. Chang, C. Felser, S.-Y. Xu, S. Jia, H. Lin, and M. Zahid Hasan, Topological chiral crystals with helicoid-arc quantum states, Nature **567**, 500–505 (2019).
[40] D. Takane, Z. Wang, S. Souma, K. Nakayama, T. Nakamura, H. Oinuma, Y. Nakata, H. Iwasawa, C. Cacho, T. Kim, K. Horiba, H. Kumigashira, T. Takahashi, Y. Ando, and T. Sato, Observation of chiral fermions with a large topological charge and associated Fermi-arc surface states in CoSi, Phys. Rev. Lett. **122**, 076402 (2019).
[41] N. B. M. Schröter, S. Stolz, K. Manna, F. de Juan, M. G. Vergniory, J. A. Krieger, D. Pei, T. Schmitt, P. Dudin, T. K. Kim, C. Cacho, B. Bradlyn, H. Borrmann, M. Schmidt, R. Widmer, V. N. Strocov, and C. Felser, Observation and control of maximal chern numbers in a chiral topological semimetal, Science **369**, 179 (2020).
[42] M. Yao, K. Manna, Q. Yang, A. Fedorov, V. Voroshnin, B. Valentin Schwarze, J. Hornung, S. Chattopadhyay, Z. Sun, S. N. Guin, J. Wosnitza, H. Borrmann, C. Shekhar, N. Kumar, J. Fink, Y. Sun, and C. Felser, Observation of giant spin-split Fermi-arc with maximal Chern number in the chiral topological semimetal PtGa, Nature Communications **11**, 2033 (2020).
[43] G. Chang, S.-Y. Xu, B. J. Wieder, D. S. Sanchez, S.-M. Huang, I. Belopolski, T.-R. Chang, S. Zhang, A. Bansil, H. Lin, and M. Z. Hasan, Unconventional chiral fermions and large topological Fermi arcs in RhSi, Phys. Rev. Lett. **119**, 206401 (2017).
[44] X. Xiao, Y. Jin, D.-S. Ma, W. Kong, J. Fan, R. Wang, and X. Wu, Realization of charge-four Weyl point in fermionic systems, Phys. Rev. B **108**, 075130 (2023).
[45] E. Witten, Three lectures on topological phases of matter, Riv. Nuovo Cim. **39**, 313 (2016).
[46] K. Hashimoto, T. Kimura, and X. Wu, Boundary conditions of Weyl semimetals, Progress of Theoretical and Experimental Physics **2017**, 053I01 (2017), [Erratum: PTEP 2019, 029201 (2019)].
[47] B. Seradjeh and M. Vennettilli, Surface spectra of Weyl semimetals through self-adjoint extensions, Phys. Rev. B **97**, 075132 (2018).
[48] D. Wawrzik, J.-S. You, J. I. Facio, J. van den Brink, and I. Sodemann, Infinite Berry curvature of Weyl Fermi arcs, Phys. Rev. Lett. **127**, 056601 (2021).
[49] R. Okugawa and S. Murakami, Dispersion of Fermi arcs in Weyl semimetals and their evolutions to Dirac cones, Phys. Rev. B **89**, 235315 (2014).
[50] Y. Liu, J. Lin, V. Wang, and J. Nara, Fermi arcs of topological surface states and Lifshitz transitions in multi-Weyl semimetals, Phys. Scripta **100**, 025939 (2025), arXiv:2107.11044 [cond-mat.mes-hall].
[51] Z. Faraei, T. Farajollahpour, and S. A. Jafari, Green's function of semi-infinite Weyl semimetals, Phys. Rev. B **98**, 195402 (2018).
[52] S. Juergens and B. Trauzettel, Exotic surface states in hybrid structures of topological insulators and Weyl semimetals, Phys. Rev. B **95**, 085313 (2017).
[53] M. Kharitonov, J.-B. Mayer, and E. M. Hankiewicz, Universality and stability of the edge states of chiral-symmetric topological semimetals and surface states of the Luttinger semimetal, Phys. Rev. Lett. **119**, 266402 (2017).
[54] Z. Zhu, G. W. Winkler, Q. Wu, J. Li, and A. A. Soluyanov, Triple point topological metals, Phys. Rev. X **6**, 031003 (2016).

[55] Y.-Q. Zhu, D.-W. Zhang, H. Yan, D.-Y. Xing, and S.-L. Zhu, Emergent pseudospin-1 Maxwell fermions with a threefold degeneracy in optical lattices, Phys. Rev. A **96**, 033634 (2017).

[56] H. Weng, C. Fang, Z. Fang, and X. Dai, Topological semimetals with triply degenerate nodal points in θ-phase tantalum nitride, Phys. Rev. B **93**, 241202 (2016).

[57] P. Tang, Q. Zhou, and S.-C. Zhang, Multiple types of topological fermions in transition metal silicides, Phys. Rev. Lett. **119**, 206402 (2017).

[58] H. Weng, C. Fang, Z. Fang, and X. Dai, Coexistence of Weyl fermion and massless triply degenerate nodal points, Phys. Rev. B **94**, 165201 (2016).

[59] A. Y. Prykhodko, E. V. Gorbar, and P. O. Sukhachov, Surface states and finite size effects in triple-fold semimetals, Journal of Physics: Condensed Matter **37**, 405002 (2025).

[60] G. Chang, S.-Y. Xu, B. J. Wieder, D. S. Sanchez, S.-M. Huang, I. Belopolski, T.-R. Chang, S. Zhang, A. Bansil, H. Lin, and M. Z. Hasan, Unconventional chiral fermions and large topological Fermi arcs in RhSi, Phys. Rev. Lett. **119**, 206401 (2017).

[61] G. Xu, H. Weng, Z. Wang, X. Dai, and Z. Fang, Chern semimetal and the quantized anomalous Hall effect in $HgCr_2Se_4$, Phys. Rev. Lett. **107**, 186806 (2011).

[62] S.-M. Huang, S.-Y. Xu, I. Belopolski, C.-C. Lee, G. Chang, T.-R. Chang, B. Wang, N. Alidoust, G. Bian, M. Neupane, D. Sanchez, H. Zheng, H.-T. Jeng, A. Bansil, T. Neupert, H. Lin, and M. Z. Hasan, New type of Weyl semimetal with quadratic double weyl fermions, Proceedings of the National Academy of Sciences **113**, 1180 (2016).

[63] B. Singh, G. Chang, T.-R. Chang, S.-M. Huang, C. Su, M.-C. Lin, H. Lin, and A. Bansil, Tunable double-Weyl fermion semimetal state in the $SrSi_2$ materials class, Scientific Reports **8**, 10540 (2018).

[64] Q. Liu and A. Zunger, Predicted realization of cubic Dirac fermion in quasi-one-dimensional transition-metal monochalcogenides, Phys. Rev. X **7**, 021019 (2017).

[65] T. Zhang, R. Takahashi, C. Fang, and S. Murakami, Twofold quadruple Weyl nodes in chiral cubic crystals, Phys. Rev. B **102**, 125148 (2020).

[66] C. Cui, X.-P. Li, D.-S. Ma, Z.-M. Yu, and Y. Yao, Charge-four Weyl point: Minimum lattice model and chirality-dependent properties, Phys. Rev. B **104**, 075115 (2021).

[67] L. Luo, W. Deng, Y. Yang, M. Yan, J. Lu, X. Huang, and Z. Liu, Observation of quadruple Weyl point in hybrid-Weyl phononic crystals, Phys. Rev. B **106**, 134108 (2022).

[68] A. Raj, S. Chaudhary, and G. A. Fiete, Photogalvanic response in multi-Weyl semimetals, Phys. Rev. Res. **6**, 013048 (2024).

[69] Y. Zhang, D. Bulmash, P. Hosur, A. C. Potter, and A. Vishwanath, Quantum oscillations from generic surface Fermi arcs and bulk chiral modes in Weyl semimetals, Scientific Reports **6**, 23741 (2016).